SCIENTIFIC REPORTS
nature research

Corrected: Author Correction

OPEN

Thickness-dependent magnetic order in CrI_3 single crystals

Yu Liu[1], Lijun Wu[1], Xiao Tong[2], Jun Li[1], Jing Tao[1], Yimei Zhu[1] & C. Petrovic[1]

Received: 14 March 2019
Accepted: 31 August 2019
Published online: 19 September 2019

Two-dimensional (2D) materials with intrinsic ferromagnetism provide unique opportunity to engineer new functionalities in nano-spintronics. One such material is CrI_3, showing long-range magnetic order in monolayer with the Curie temperature (T_c) of 45 K. Here we study detailed evolution of magnetic transition and magnetic critical properties in response to systematic reduction in crystal thickness down to 50 nm. Bulk T_c of 61 K is gradually suppressed to 57 K, however, the satellite transition at $T^* = 45$ K is observed layer-independent at fixed magnetic field of 1 kOe. The origin of T^* is proposed to be a crossover from pinning to depinning of magnetic domain walls. The reduction of thickness facilitates a field-driven metamagnetic transition around 20 kOe with out-of-plane field, in contrast to the continuous changes with in-plane field. The critical analysis around T_c elucidates the mean-field type interactions in microscale-thick CrI_3.

Layered materials, when thinned to atomic limits in 2D exhibit novel properties, different from the bulk counterpart. Recent discoveries of intrinsic 2D ferromagnetism in atomically thin CrI_3 and $Cr_2Ge_2Te_6$ open up new opportunities for studying fundamental 2D magnetism and show great potential in spintronic applications[1–3]. CrI_3 and $Cr_2Ge_2Te_6$ are ferromagnetic (FM) below $T_c \sim 61$ K in bulk[4–6]. First-principle calculations predict a robust 2D ferromagnetism with $T_c \sim 57.2$ or 106 K in monolayer $Cr_2Ge_2Te_6$[7,8], However, the scanning magneto-optic Kerr microscopy experiment shows that the T_c monotonically decreases with decreasing thickness, showing 30 K in bilayer and the absence of T_c in monolayer[3].

In bulk CrI_3, the Cr atoms in each layer form a honeycomb structure, and each Cr atom is surrounded by six I atoms in an octahedral coordination [Fig. 1(a)]. In contrast to $Cr_2Ge_2Te_6$, ferromagnetism in CrI_3 persists in monolayer with T_c of 45 K[2]. Intriguingly, the magnetism in CrI_3 is layer-dependent, from FM in monolayer to antiferromagnetic (AFM) in bilayer, and back to FM in trilayer, providing great opportunities for designing magneto-optoelectronic devices[2]. The monolayer CrI_3 can be described by the Ising model[2,9]. Remarkably, the electrostatic doping can modify the saturation magnetization, the coercive force, and the T_c in monolayer as well as change the interlayer magnetic order in bilayer CrI_3[10,11]. In addition, giant tunneling magnetoresistance is observed in few-layer CrI_3, exhibiting multiple states as a function of magnetic field[12–15]. This highlights CrI_3 as a potential magnetic tunnel barrier for van der Waals heterostructure spintronic devices and also shows demand for magnetic order investigation at all length scales from bulk to monolayer.

Here we report a detailed study of thickness-dependent magnetic transition and critical behavior in CrI_3. An additional satellite transition at T^* was observed just below T_c. The value of T^* is found thickness-independent at fixed magnetic field, in contrast to gradually suppressed T_c with reduction in thickness. Thin CrI_3 crystals show an increase in coercive field and distinct field-driven metamagnetic transition around 20 kOe with out-of-plane field but not in-plane field. The critical behavior suggests the long-range mean-field type interactions in mesoscale-thick CrI_3 crystals.

Methods

Bulk CrI_3 single crystals were fabricated by the chemical vapor transport method and characterized as described previously[16]. A series of thicknesses were obtained step-by-step mechanical exfoliating bulk crystal down to nanometer scale [Fig. 1(b,c)]. Considering the reactivity of thin CrI_3 flakes, all the samples were prepared in an argon-filled glove-box and protected using scotch tape on both sides when transferring for magnetization measurement. The dc magnetization was measured in Quantum Design MPMS-XL5 system. An optical microscopy equipped with 100× objective lens in Witec alpha 300 confocal Raman microscope was used for imaging the cross-section of S2 sample to determine its thickness. Transmission electron microscopy (TEM) sample of S3 was

[1]Condensed Matter Physics and Materials Science Department, Brookhaven National Laboratory, Upton, New York, 11973, USA. [2]Center for Functional Nanomaterials, Brookhaven National Laboratory, Upton, New York, 11973, USA. Correspondence and requests for materials should be addressed to Y.L. (email: yuliu@bnl.gov) or C.P. (email: petrovic@bnl.gov)

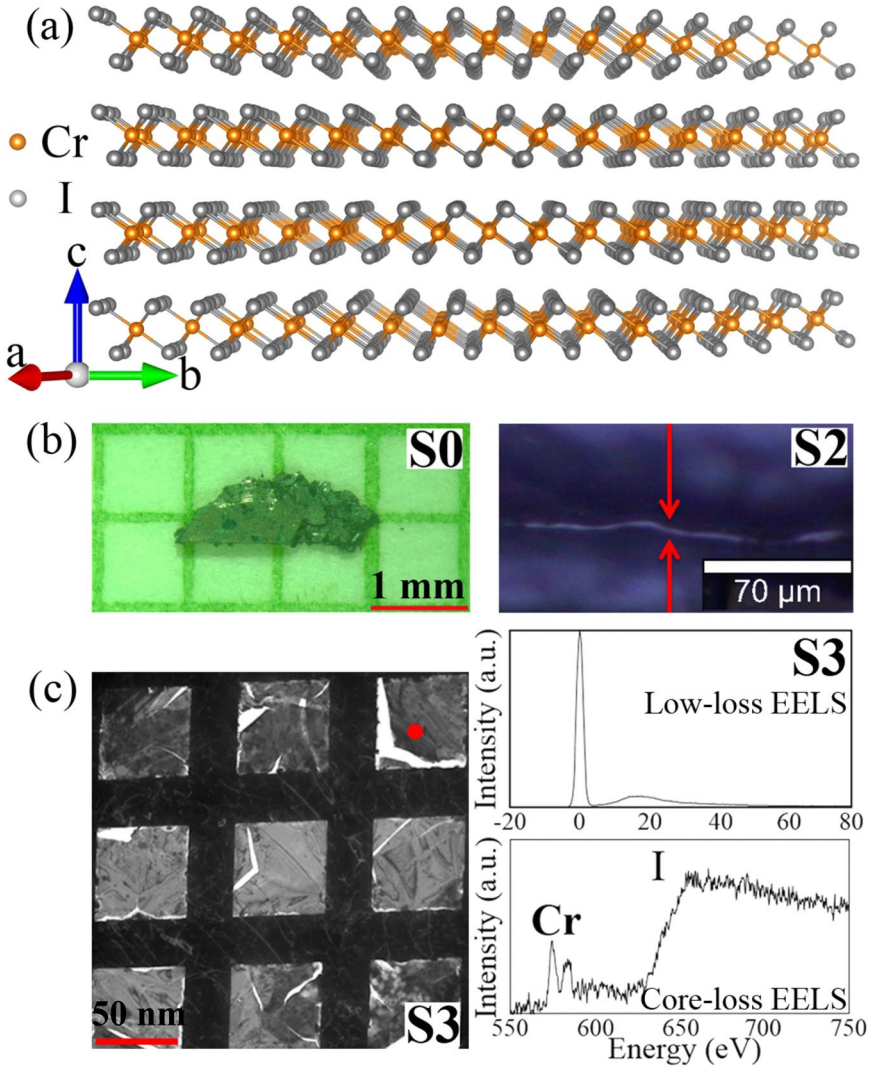

Figure 1. (**a**)Low temperature structure of CrI_3 in the $R\bar{3}$ space group. (**b**) Optical microscopy of bulk S0 sample (thickness ~100 μm) and cross-section of S2 sample (thickness ~2 μm). (**c**) Transmission electron microscopy (TEM) image of S3 sample in Cu grid along with the low-loss and core-loss electron energy loss spectra (EELS) taken from top right area marked by red circle. The thickness of S3 was calculated from the low-loss EELS based on log-ratio method in Digital Micrograph program to be 44 nm. The average thickness for many areas measured is 49 ± 8 nm.

prepared by putting the exfoliated S3 sample in Cu grid. The thickness (t) of S3 sample was measured by the low loss EELS spectrum in JEM-ARM200F microscope [Fig. 1(c)], $t = ln(I_t/I_0) \times \lambda$, where I_0 and I_t are integrated EELS signal intensity under the zero-loss peak and the total spectrum, respectively; λ is a total mean free path for all inelastic scattering which can be calculated based on the composition of the sample[17].

Results and Discussion

Figure 2(a–d) present the temperature-dependent magnetization $M(T)$ with zero-field cooling (ZFC) and field-cooling (FC) modes measured in out-of-plane field $H = 1$ kOe for the samples (S0–S3) with typical thickness from 100 μm to 50 nm. There is an apparent increase in $M(T)$, in line with the paramagnetic (PM) to FM transition[1]. The T_c can be determined from the minima of the first derivative of the $M(T)$ curves [insets in Fig. 2(a–d)]. Given the large magnetocrystalline anisotropy in CrI_3[18], the divergence of ZFC and FC curves is observed below T_c in $H = 1$ kOe. With subsequent reduction of crystal thickness this discrepancy tends to be larger, indicating an increasing anisotropy in thin crystals. Intriguingly, an additional satellite transition T^* just below T_c is observed. A similar phenomenon was also observed in Fe_3GeTe_2, arising from the emergence of antiparallel spin arrangement along the c axis between different Fe_3Ge layers[19]. This satellite transition T^* is defined by the maxima of the first derivative of the $M(T)$ curves [insets in Fig. 2(b–d)], which is more apparent in thinner crystal. The thickness dependence of T_c and T^* is summarized in Fig. 2(e). The T_c shows linear decrease with logarithm of thickness. In contrast, the T^* seems thickness-independent and shows a value of 45 K identical to the T_c in monolayer measured by magneto-optic Kerr microscopy in $H = 1.5$ kOe[2]. The isothermal magnetization at $T = 2$ K for the

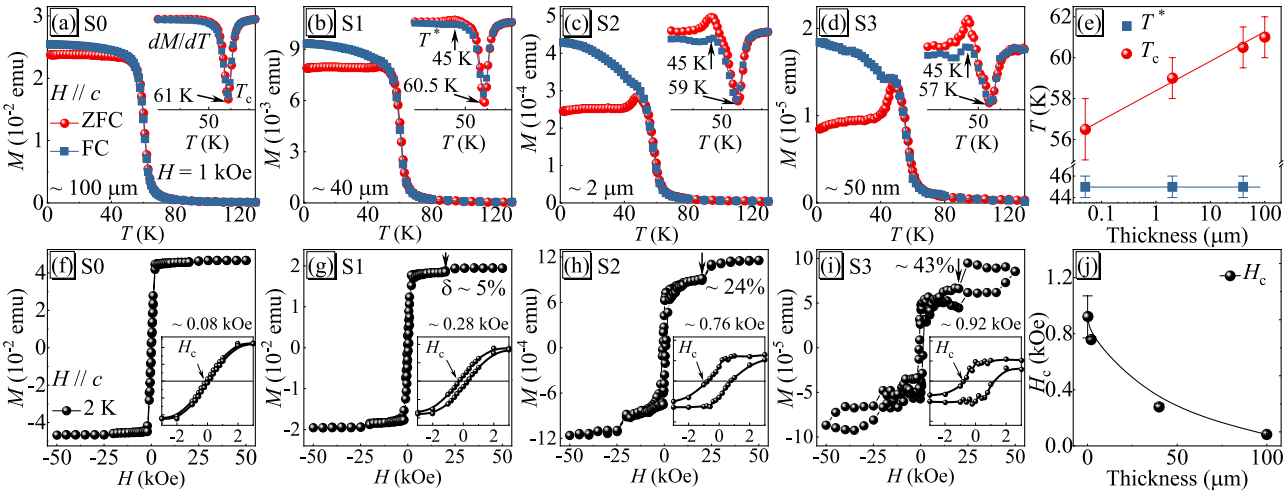

Figure 2. (**a–d**) Temperature dependence of magnetization for CrI_3 at various crystal thicknesses measured with $H//c$ at 1 kOe. Insets show the first derivative of the $M(T)$ curves. (**e**) Thickness-dependent T^* and T_c. (**f–i**) Isothermal magnetization at $T = 2$ K for corresponding S0-S3 samples. Insets show the enlarged low field part and the derived coercive field H_c. (**j**) Thickness dependence of H_c.

corresponding samples is shown in Fig. 2(f–i). With $H//c$, the magnetization of bulk CrI_3 crystal saturates at a relatively low magnetic field $H \sim 2$ kOe and in line with the previous reports[1,16]. With reduction of thickness, there is an increase of coercive field H_c as shown in insets of Fig. 2(f–i), from about 80 Oe for S0 sample to 920 Oe for S3 sample, still identified as a relatively soft ferromagnet. It is interesting to note that an apparent magnetization jump around $H \sim 20$ kOe is observed in thin crystals. The calculated value $\delta = [M(25kOe) - M(20kOe)]/M(20kOe)$ increases from 5% for S1 to 43% for S3. This field-driven metamagnetic transition is first identified by the step-like change of magnetization in the hysteresis curves, which is similar with the giant tunneling magnetoresistance step around the same field observed in few-layer devices[15]. The tunneling magnetoresistance step in few-layer devices is attributed to spin filtering effect arising from collapse of interlayer AFM in thin CrI_3[12–15]. Above this critical field, a fully spin polarized FM state is reached in S0–S2 samples, however, a large hysteresis is observed in S3 sample.

To well understand the nature of magnetism in CrI_3 and its properties from bulk to monolayer, we then focus on the S2 sample with mesoscale thickness of 2 μm. Figure 3 shows the temperature- and field-dependent magnetization $M(T,H)$ with out-of-plane and in-plane fields, respectively. The $M(T)$ is nearly isotropic in $H = 50$ kOe, whilst anisotropic magnetic response is observed in low fields. In $H = 10$ kOe, a monotonic increase of $M(T)$ with decreasing temperature is observed for $H//c$ [Fig. 3(a)], however, the $M(T)$ decreases with decreasing temperature below 50 K for $H//ab$ [Fig. 3(d)]. Similar feature was also observed in bulk CrI_3 crystal, associated with its temperature dependent magnetocrystalline anisotropy[18,20]. The satellite transition T^* reveals itself by the emergence of a weak kink in the dM/dT curve with $H = 10$ kOe. With decreasing field, the magnetic anisotropy results in larger divergence between ZFC and FC magnetization and a more abrupt satellite transition, as shown in Fig. 3(b,e). Both T_c and T^* are field-dependent but with an opposite tendency, i.e., with decreasing field the T_c decreases whereas the T^* gradually increases. The isothermal magnetization at 2 K increases discretely for out-of-plane field [Fig. 3(c)], but monotonically for in-plane field [Fig. 3(f)]. Although an A-type AFM ground state was proposed in few-layer devices[15], a FM ground state is still expected in S2 sample with thickness ~2 μm. Therefore, the field-driven metamagnetic transition is most likely caused by a movement or depinning of magnetic domains, rather than flipping the spins from an antiparallel to a parallel configuration. A crossover from pinning to depinning of magnetic domain walls is also proposed as the reason for the satellite T^* kink. When the sample is cooled in zero field, the magnetic domains start to be pinned below the crossover temperature T^*. Small applied field at base temperature is insufficient to move the pinned domains. With increasing temperature, thermal fluctuations gradually weaken the pinning force and finally completely depin the domains above T^*. This also explains why the T^* kink is more apparent in the ZFC curves. In the FC process the domains are always pinned with the effective FM moment aligned along the cooling field.

Near a second-order phase transition, the free energy of a ferromagnet $F_m(M) = F_m(0) + \frac{1}{2}aM^2 + \frac{1}{4}bM^4 + \ldots - HM$. By $\partial F_m(M)/\partial M = 0$, the equation of state is obtained as $H/M = a + bM^2$ for the behavior of magnetization near T_c. According to the scaling hypothesis, the spontaneous magnetization M_s below T_c, the inverse initial susceptibility H/M above T_c, and the $M(H)$ at T_c can be characterized by a series of critical exponents[21]:

$$M_s(T) = M_0(-\varepsilon)^{\beta}, \varepsilon < 0, T < T_c, \quad (1)$$

$$H/M(T) = (h_0/m_0)\varepsilon^{\gamma}, \varepsilon > 0, T > T_c, \quad (2)$$

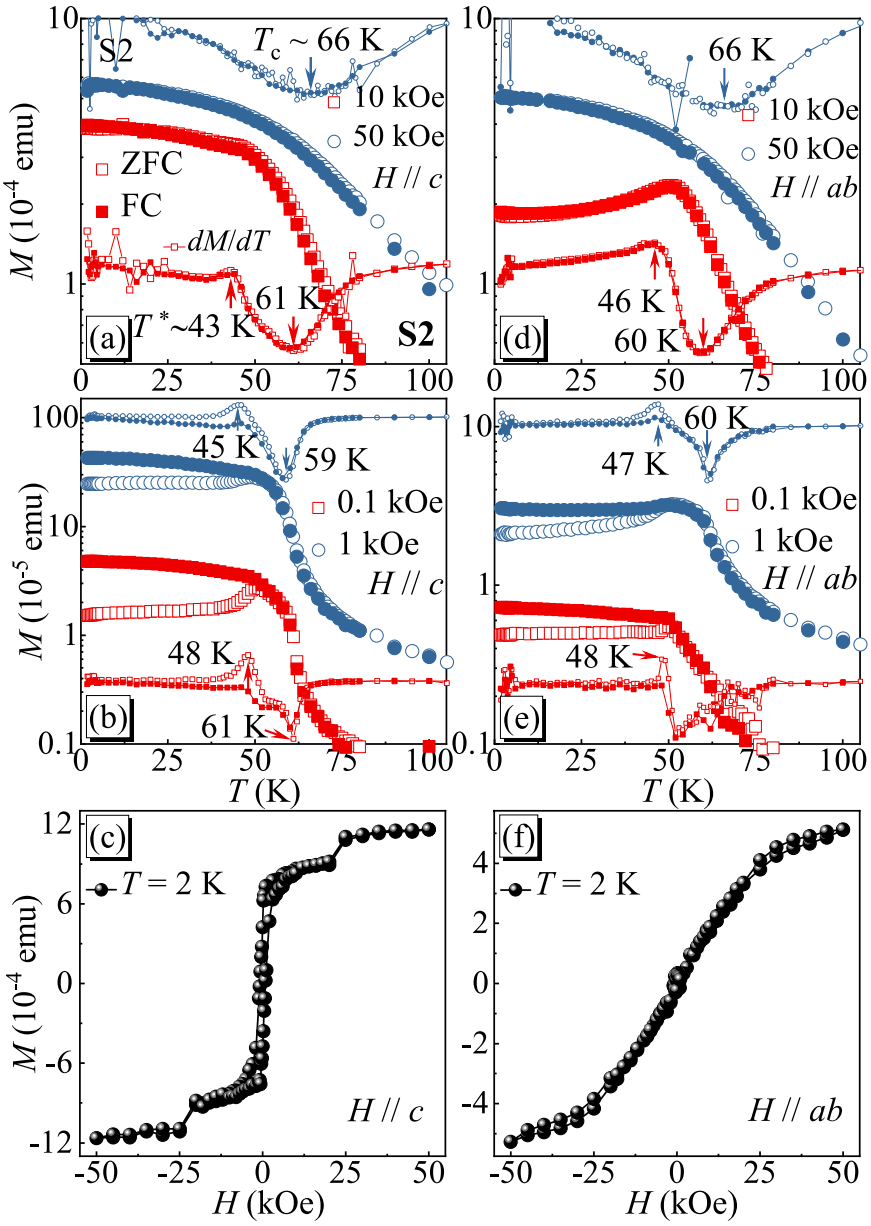

Figure 3. (**a,b**)Temperature-dependent magnetization measured at various magnetic fields and (**c**) field-dependent magnetization measured at $T = 2$ K for $H//c$. (**d,e**) Temperature-dependent magnetization measured at various magnetic fields and (**f**) field-dependent magnetization measured at $T = 2$ K for $H//ab$.

$$M = DH^{1/\delta},\ \varepsilon = 0,\ T = T_c, \tag{3}$$

where M_0, h_0/m_0, D and $\varepsilon = (T - T_c)/T_c$ are the critical amplitudes and the reduced temperature, respectively[22].

The isothermal magnetization curves with out-of-plane field are depicted in Fig. 4(a,b). The magnetization jump gradually moves to lower field and finally disappears at 50 K for S2. The Arrott plot of M^2 vs H/M [Fig. 4(c)], with $\beta = 0.5$ and $\gamma = 1.0$[23,24], gives a set of quasi-straight lines and the isotherm at T_c pass through the origin, suggesting the mean-field type magnetic interactions in S2 sample. In addition, the positive slope of the straight lines indicates that it is a second-order transition based on the Banerjee's criterion[25]. The Arrot-Noaks equation of state gives a general modified Arrott plot $(H/M)^{1/\gamma} = a\varepsilon + bM^{1/\beta}$, where a and b are constants[26]. Taking into consideration the three-dimensional (3D) critical behavior in bulk CrI_3 (S0 sample)[16], and 2D Ising-like in monolayer[2], a set of possible exponents belonging to different models are used to build the modified Arrott plots[27]. Comparison the normalized slope ($NS = S(T)/S(T_c)$) with ideal value "1" can determine the most suitable model, where $S(T) = dM^{1/\beta}/d(H/M)^{1/\gamma}$. Figure 4(d) presents the NS vs T curves for indicated models, confirming that the mean-field model is the best and the 2D Ising model shows the largest deviation. That is to say, the critical behavior of mesoscale S2 sample is quite different when compared to bulk and monolayer[2,16].

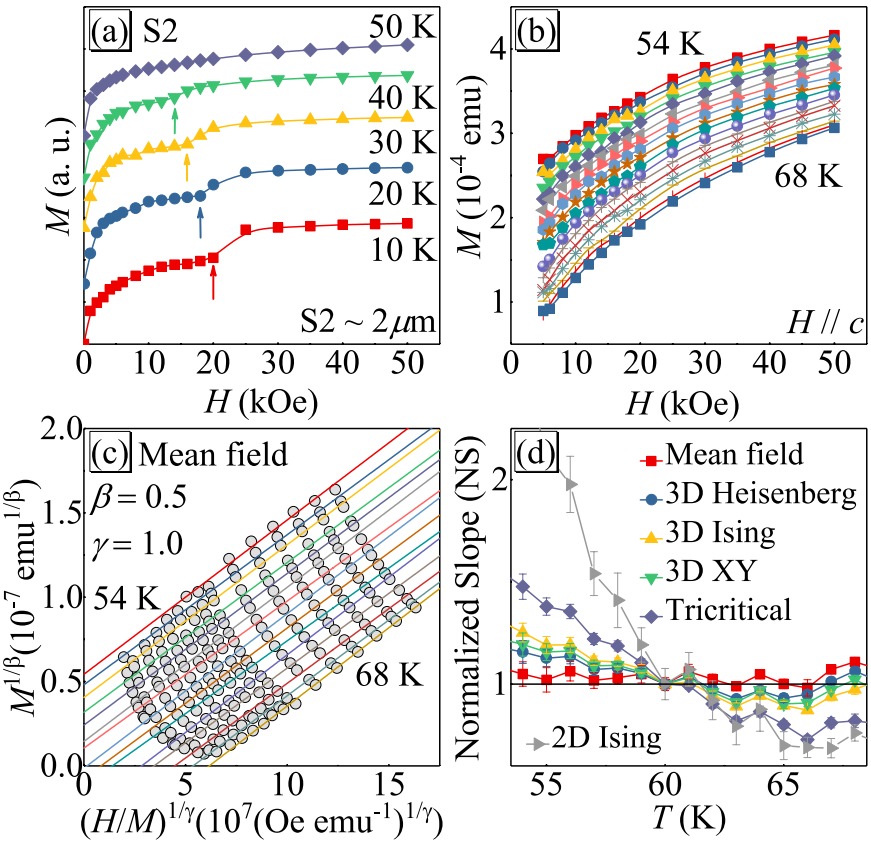

Figure 4. (**a,b**) Initial isothermal magnetization at various temperatures with out-of-plane field. (**c**) The Arrott Plot of S2 sample with $\beta = 0.5$ and $\gamma = 1.0$. (**d**) Temperature-dependent $NS = S(T)/S(T_c)$ for indicated models.

The linearly extrapolated M_s and H/M are plotted from in Fig. 5(a). The solid lines are fitted lines according to Eqs (1) and (2). The precise critical exponents $\beta = 0.45(2)$, with $T_c = 60.9(2)$ K, and $\gamma = 0.90(8)$, with $T_c = 60.6(2)$ K, are obtained, close to the parameters of mean-field model. According to Eq. (3), the $M(H)$ at T_c should be a straight line in log-log scale with the slope of $1/\delta$ [inset in Fig. 5(a)]. Such fitting yields $\delta = 3.12(3)$ for $T = 60$ K and 2.88(4) for $T = 61$ K, respectively. The Kouvel-Fisher (KF) method can be used to double check the obtained critical exponents,

$$\frac{M_s(T)}{dM_s(T)/dT} = \frac{T - T_c}{\beta}, \tag{4}$$

$$\frac{H/M(T)}{d[H/M(T)]/dT} = \frac{T - T_c}{\gamma}, \tag{5}$$

where $M_s/(dM_s/dT)$ and $(H/M)/[d(H/M)/dT]$ are linear in T and the slopes are $1/\beta$ and $1/\gamma$, respectively[28]. Such fitting gives $\beta = 0.41(2)$, with $T_c = 60.5(3)$ K, and $\gamma = 0.87(8)$, with $T_c = 60.7(3)$ K, respectively, in line with the values obtained by the modified Arrott plot.

The reliability of obtained critical exponents β, γ, δ, and T_c can be further checked by a scaling analysis. Near the critical region, the magnetic equation of state can be expressed as

$$M(H, \varepsilon) = \varepsilon^{\beta} f_{\pm}(H/\varepsilon^{\beta+\gamma}), \tag{6}$$

where $f_{\pm}$ is the regular function with f_- for $T < T_c$, and f_+ for $T > T_c$, respectively. This equation can be further expressed as $m = f_{\pm}(h)$, where $m \equiv \varepsilon^{-\beta} M(H, \varepsilon)$ and $h \equiv \varepsilon^{-(\beta+\gamma)} H$ are the rescaled magnetization and magnetic field, respectively. Figure 5(c) presents the scaled m vs h in log-log scale, falling on two separate branches above and below T_c, confirming the true scaling treatment and the intrinsic critical values of β, γ, and δ. The scaling equation of state can also be expressed as

$$\frac{H}{M^{\delta}} = k\left(\frac{\varepsilon}{H^{1/\beta}}\right), \tag{7}$$

where the $MH^{-1/\delta}$ vs $\varepsilon H^{-1/(\beta\delta)}$ should collapse into a single curve with the T_c locating at horizontal zero point [Fig. 5(d)].

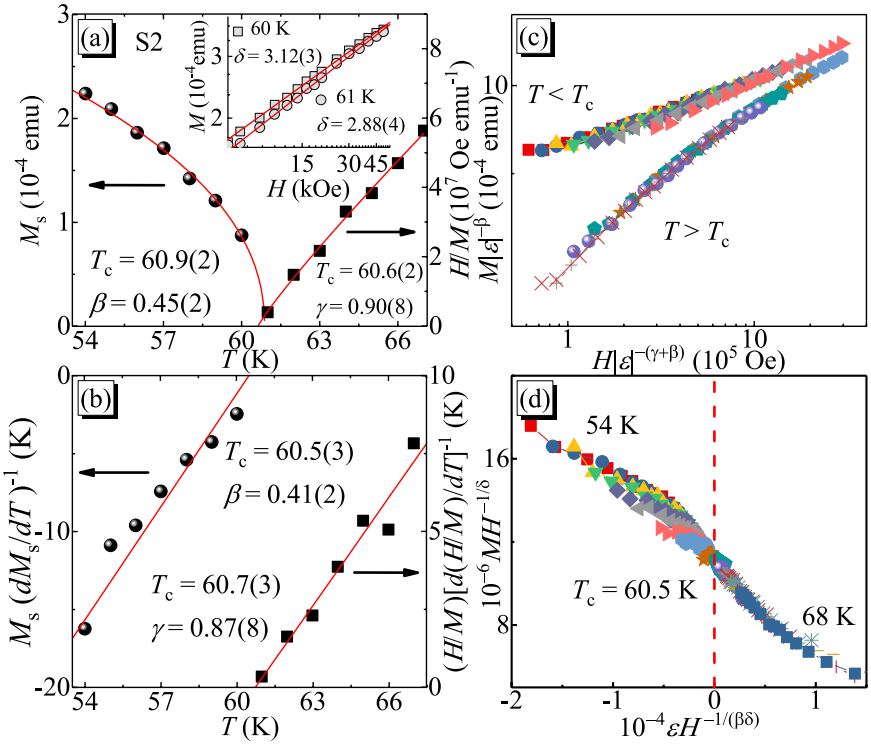

Figure 5. (**a**)Temperature-dependent M_s (left) and H/M (right) with solid fitting curves. Inset shows the isotherms $M(H)$ in log-log scale near T_c with linear fitting curves. (**b**) Temperature-dependent $M_s(dM_s/dT)^{-1}$ (left) and $(H/M)[d(H/M)/dT)]^{-1}$ (right) with linear fitting curves. (**c**) Scaling plot of m vs h with $m \equiv \varepsilon^{-\beta}M(H, \varepsilon)$ and $h \equiv \varepsilon^{-(\beta+\gamma)}$H, respectively. (**d**) $MH^{-1/\delta}$ vs $\varepsilon H^{-1/(\beta\delta)}$.

Thickness	Theoretical model	Reference	Technique	T_c (K)	β	γ	δ
S0 ~100 μm		[16]	MAP	60.45 (3)/60.38 (6)	0.284 (3)	1.146 (11)	5.04 (1)
		[16]	KFP	60.05 (13)/60.43 (4)	0.260 (4)	1.136 (6)	5.37 (4)
		[16]	CI	60			5.32 (2)
	3D Heisenberg	[29]	Theory		0.365	1.386	4.8
	3D XY	[29]	Theory		0.345	1.316	4.81
	3D Ising	[29]	Theory		0.325	1.24	4.82
	Tricritical mean field	[27]	Theory		0.25	1.0	5
S2 ~2 μm		This work	MAP	60.9 (2)/60.0 (2)	0.45 (2)	0.90 (8)	3.00 (9)
		This work	KFP	60.5 (3)/60.7 (3)	0.41 (2)	0.87 (8)	3.12 (9)
		This work	CI	60			2.88 (4)
		This work	CI	61			3.12 (3)
monolayer	Mean field	[21]	Theory		0.5	1.0	3.0
		[2]	MOK	45			
	2D Ising	[27]	Theory		0.125	1.75	15

Table 1. The critical exponents of CrI_3 (S0 and S2) with different thickness obtained by various methods such as the modified Arrott plot (MAP), the Kouvel-Fisher plot (KFP), the critical isotherm (CI) and the magneto-optical Kerr (MOK) effect, in comparison with different theoretical models.

The critical exponents of CrI_3 (S0 and S2) with different thickness are listed in Table 1 for comparison with the theoretical models[2,16,21,27,29]. For a 2D magnet, the value of critical exponent β should be within a window $\sim 0.1 \leq \beta \leq 0.25$[30]. As we can see, the critical exponents of bulk CrI_3 crystal (S0) are between the values of theoretical tricritical mean-field and 3D Ising model, exhibiting a clear 3D critical phenomenon, in contrast to $Cr_2(Si,Ge)_2Te_6$ showing 2D Ising-like behavior[31,32]. The monolayer CrI_3 is claimed as a 2D Ising-like ferromagnetism as a result of large magnetic anisotropy removing the Mermin-Wagner restriction[2,33]. However, the critical exponents of β, γ, and δ for mesoscale CrI_3 (S2) are well fit with the mean-field model (Table 1), which is quite different from the behavior in bulk and monolayer. It should be noted that the precise value of T_c for S2 almost equals to $T_c = 61$ K for S0 based on the critical analysis, in contrast to the strong thickness dependence of β, γ, and

δ. We assume that the T_c of 45 K in monolayer is most likely stabilized by the satellite transition ($T^* \sim 45$ K) in bulk CrI_3, calling for further in-depth theoretical study.

Conclusion

In summary, we have investigated the thickness-dependent magnetism in CrI_3 from bulk to 50 nm thickness. In addition to suppression of bulk T_c, we observe an additional satellite transition T^* at 45 K which is independent of thickness and corresponds to the T_c observed in monolayer. Analysis of critical behavior shows mean-field interactions in mesoscale-thick CrI_3, in contrast to that in bulk and monolayer, which is helpful to understand the nature magnetism in in CrI_3 and is of great importance for future magneto-optoelectronic devices.

References

1. McGuire, M. A., Dixit, H., Cooper, V. R. & Sales, B. C. Coupling of Crystal Structure and Magnetism in the Layered, Ferromagnetic Insulator CrI_3. *Chem. Mater.* **27**, 612, https://doi.org/10.1021/cm504242t (2015).
2. Huang, B. *et al.* Layer-dependent ferromagnetism in a van der Waals crystal down to the monolayer limit. *Nature* **546**, 270, https://doi.org/10.1038/nature22391 (2017).
3. Gong, C. *et al.* Discovery of intrinsic ferromagnetism in two-dimensional van der Waals crystals. *Nature* **546**, 265, https://doi.org/10.1038/nature22060 (2017).
4. Carteaux, V., Brunet, D., Ouvrard, G. & André, G. Crystallographic, magnetic and electronic structures of a new layered ferromagnetic compound $Cr_2Ge_2Te_6$. *J. Phys.: Condens. Matter* **7**, 69, https://doi.org/10.1088/0953-8984/7/1/008 (1995).
5. Casto, L. D. *et al.* Strong spin-lattice coupling in $CrSiTe_3$. *APL Mater* **3**, 041515, https://doi.org/10.1063/1.4914134 (2015).
6. Zhang, X. *et al.* Magnetic anisotropy of the single-crystalline ferromagnetic insulator $Cr_2Ge_2Te_6$. *Jpn. J. Appl. Phys.* **55**, 033001, https://doi.org/10.7567/JJAP.55.033001 (2016).
7. Li, X. X. & Yang, J. L. $CrXTe_3$ (X = Si, Ge) nanosheets: two dimensional intrinsic ferromagnetic semiconductors. *J. Mater. Chem. C* **2**, 7071, https://doi.org/10.1039/c4tc01193g (2014).
8. Sivadas, N., Daniels, M. W., Swendsen, R. H., Okamoto, S. & Xiao, D. Magnetic ground state of semiconducting transition-metal trichalcogenide monolayers. *Phys. Rev. B* **91**, 235425, https://doi.org/10.1103/PhysRevB.91.235425 (2015).
9. Griffiths, R. B. Peierls Proof of Spontaneous Magnetization in a Two-Dimensional Ising Ferromagnet. *Phys. Rev* **136**, A437 (1964).
10. Jiang, S., Li, L., Wang, Z., Mak, K. F. & Shan, J. Controlling magnetism in 2D CrI_3 by electrostatic doping. *Nat. Nanotech.* **13**, 549, https://doi.org/10.1038/s41565-018-0135-x (2018).
11. Huang, B. *et al.* Electrical control of 2D magnetism in bilayer CrI_3. *Nat. Nanotech* **13**, 544, https://doi.org/10.1038/s41565-018-0121-3 (2018).
12. Song, T. *et al.* Giant tunneling magnetoresistance in spin-filter van der Waals heterostructures. *Science* **360**, 1214, https://doi.org/10.1126/science.aar4851 (2018).
13. Klein, D. R. *et al.* Probing magnetism in 2D van der Waals crystalline insulators via electron tunneling. *Science* **360**, 1218, https://doi.org/10.1126/science.aar3617 (2018).
14. Wang, Z. *et al.* Very large tunneling magnetoresistance in layered magnetic semiconductor CrI_3. *Nat. Commun.* **9**, 2516, https://doi.org/10.1038/s41467-018-04953-8 (2018).
15. Kim, H. H. *et al.* One Million Percent Tunnel Magnetoresistance in a Magnetic van der Waals Heterostructure. *Nano Lett.* **18**, 4885, https://doi.org/10.1021/acs.nanolett.8b01552 (2018).
16. Liu, Y. & Petrovic, C. Three-dimensional magnetic critical behavior in CrI_3. *Phys. Rev. B* **97**, 014420, https://doi.org/10.1103/PhysRevB.97.014420 (2018).
17. Egerton, R. F. *Electron Energy-Loss Spectroscopy in the Electron Microscope* (Plenum Press, New York, 1996).
18. Richter, N. *et al.* Temperature-dependent magnetic anisotropy in the layered magnetic semiconductors CrI_3 and $CrBr_3$. *Phys. Rev. Materials* **2**, 024004, https://doi.org/10.1103/PhysRevMaterials.2.024004 (2018).
19. Yi, J. *et al.* Competing antiferromagnetism in a quasi-2D itinerant ferromagnet: Fe_3GeTe_2. *2D Mater* **4**, 011005, https://doi.org/10.1088/2053-1583/4/1/011005 (2016).
20. Liu, Y. & Petrovic, C. Anisotropic magnetocaloric effect in single crystals of CrI_3. *Phys. Rev. B* **97**, 174418, https://doi.org/10.1103/PhysRevB.97.174418 (2018).
21. Stanley, H. E. *Introduction to Phase Transitions and Critical Phenomena* (Oxford U. P., London and New York, 1971).
22. Fisher, M. E. The theory of equilibrium critical phenomena. *Rep. Prog. Phys.* **30**, 615 (1967).
23. Arrott, A. Criterion for Ferromagnetism from Observations of Magnetic Isotherms. *Phys. Rev. B* **108**, 1394, https://doi.org/10.1103/PhysRev.108.1394 (1957).
24. Lin, J. C. *et al.* Unusual ferromagnetic critical behavior owing to short-range antiferromagnetic correlations in antiperovskite $Cu_{1-x}NMn_{3+x}$ ($0.1 \leq x \leq 0.4$). *Sci. Rep* **5**, 7933, https://doi.org/10.1038/srep07933 (2015).
25. Banerjee, B. K. On a generalised approach to first and second order magnetic transitions. *Phys. Lett.* **12**, 16, https://doi.org/10.1016/0031-9163(64)91158-8 (1964).
26. Arrott, A. & Noakes, J. E. Approximate Equation of State For Nickel Near its Critical Temperature. *Phys. Rev. Lett.* **19**, 786, https://doi.org/10.1103/PhysRevLett.19.786 (1967).
27. LeGuillou, J. C. & Zinn-Justin, J. Critical exponents from field theory. *Phys. Rev. B* **21**, 3976, https://doi.org/10.1103/PhysRevB.21.3976 (1980).
28. Kouvel, J. S. & Fisher, M. E. Detailed Magnetic Behavior of Nickel Near its Curie Point. *Phys. Rev* **136**, A1626, https://doi.org/10.1103/PhysRev.136.A1626 (1964).
29. Kaul, S. N. Static critical phenomena in ferromagnets with quenched disorder. *J. Magn. Magn. Mater.* **53**, 5, https://doi.org/10.1016/0304-8853(85)90128-3 (1985).
30. Taroni, A., Bramwell, S. T. & Holdsworth, P. C. W. Universal window for two-dimensional critical exponents. *J. Phys.: Condens. Matter* **20**, 275233, https://doi.org/10.1088/0953-8984/20/27/275233 (2008).
31. Liu, Y. & Petrovic, C. Critical behavior of quasi-two-dimensional semiconducting ferromagnet $Cr_2Ge_2Te_6$. *Phys. Rev. B* **96**, 054406, https://doi.org/10.1103/PhysRevB.96.054406 (2017).
32. Lin, G. T. *et al.* Critical behavior of two-dimensional intrinsically ferromagnetic semiconductor CrI_3. *Appl. Phys. Lett.* **112**, 072405, https://doi.org/10.1063/1.5019286 (2018).
33. Mermin, N. D. & Wagner, H. Absence of Ferromagnetism or Antiferromagnetism in One- or Two-Dimensional Isotropic Heisenberg Models. *Phys. Rev. Lett.* **17**, 1133, https://doi.org/10.1103/PhysRevLett.17.1133 (1966).

Acknowledgements

Work at Brookhaven National Laboratory was supported by US DOE, Office of Science, Office of Basic Energy Sciences under contract DE-SC0012704.

Author Contributions

C.P. initiated the study, designed research and supervised the project. Y.L. synthesized crystals and performed magnetization measurements. X.T. performed optical microscopy study. L.W., J.L., J.T. and Y.Z. contributed TEM and EELS measurements. Y.L. and C.P. organized and wrote the paper with input from all collaborators. This manuscript reflects the contribution and ideas of all authors.

Additional Information

Competing Interests: The authors declare no competing interests.

Publisher's note Springer Nature remains neutral with regard to jurisdictional claims in published maps and institutional affiliations.

Open Access This article is licensed under a Creative Commons Attribution 4.0 International License, which permits use, sharing, adaptation, distribution and reproduction in any medium or format, as long as you give appropriate credit to the original author(s) and the source, provide a link to the Creative Commons license, and indicate if changes were made. The images or other third party material in this article are included in the article's Creative Commons license, unless indicated otherwise in a credit line to the material. If material is not included in the article's Creative Commons license and your intended use is not permitted by statutory regulation or exceeds the permitted use, you will need to obtain permission directly from the copyright holder. To view a copy of this license, visit http://creativecommons.org/licenses/by/4.0/.

© The Author(s) 2019